

Template-Free N-Doped Hierarchical Porous Carbon from Azobenzene-Interconnected Polyimide for Ultra-Stable Supercapacitor Electrodes

He Zhou,^[a, b] Yunjiao Gu,^{*[a]} Fenghua Liu,^[a] and Weiping Wu^{*[a]}

Facile preparation of N-doped hierarchical porous carbon (NHPC) materials with controllable composition and porosity is crucial for advancing the development of high-performance supercapacitors. In this study, a new NHPC has been created by first using the one-pot synthesis of *in-situ* dual-crosslinking azobenzene-interconnected polyimide precursors from ingeniously designed three monomers, followed by carbonization activation. We have found that during the polymer precursor synthesis stage, the incorporation of azobenzene into the polyimide network is the key, as it not only functions as an *in-situ* N-rich source but also enables the template-free formation of a multi-scale micro/nanoporous carbon structure, which is

critical for enhancing electrical performance and stability. The resulting N-doped carbon material with a specific surface area of $900.1 \text{ m}^2 \text{ g}^{-1}$ exhibits a maximum capacitance of 179.2 F g^{-1} in a three-electrode configuration. The assembled symmetric supercapacitor using NHPC as the electrode delivers a good energy density (18.0 Wh kg^{-1}) and power density (799.51 W kg^{-1}) at a current density of 1 A g^{-1} . Most notably, the NHPC electrode retains an efficiency of 113.5% without decrease, demonstrating impressive cycling stability, even after 5000 charge-discharge cycles at 10 A g^{-1} . This study offers a new and universal molecular design methodology for advancing supercapacitor materials with outstanding cycling stabilities.

1. Introduction

Clean energy resources and related power storage technologies are vital for achieving global sustainability goals.^[1,2] Supercapacitors, recognized for their fast charge-discharge capability and high power density, have garnered significant attention over the decades as eco-friendly energy storage devices.^[3–6] They are classified into two categories: electrical double-layer capacitors (EDLCs) operate through ion adsorption and desorption occurring at the interface between the electrolyte and electrode,^[7–9] while Faraday pseudocapacitors, which involve reversible ion insertion or redox reactions on the electrode surface.^[10–12] Heteroatom-doped nitrogen-doped porous carbons (N-doped PCs), which enhance energy storage by combining EDLC behavior with additional redox activity from heteroatoms, are pushing the boundaries of energy storage capacity and energy density.^[13–15] However, current N-doped carbon electrodes still suffer from performance degradation, such as unsatisfactory cycling retention and evident efficiency

decrease at high current densities, underscoring the need for the development of high-quality supercapacitors with outstanding stability.

Currently, adjusting the structure of N-containing polymer precursors and modulating the resulting porosity after carbonization are two effective directions to overcome the above issue. In terms of the first direction, while biomass-derived carbons are abundant and renewable, synthetic polymer-based carbons offer precise molecular tailoring, which can facilitate a deeper understanding of the interplay between material structures and electrical performances.^[16] Sheng et al. successfully synthesized poly (vinyl chloride)-derived N-doped carbon nanosheets with hierarchical porosity by a one-pot carbonization process,^[15] achieving a specific capacitance of 347 F g^{-1} at 0.5 A g^{-1} . Du et al. developed a co-assembly method for the controlled preparation of Nitrogen-doped hollow mesoporous carbon spheres (N-HMCS) with different morphologies,^[17] and the N-HMCS exhibited excellent electrochemical properties when used as electrode materials in supercapacitors. However, most of these N-doped porous carbon is limited to single-crosslinking polymer networks before carbonization, which is unfavorable for molecular diversity as polymer precursors, and the as-prepared electrodes still exhibit performance losses under high current.

Porosity modulation is another important issue. First of all, previous focus on high specific surface areas with dense and all small micropores (pore size $< 2 \text{ nm}$) may not always be advantageous, especially at higher current densities and during extended cycling. It increases the ion diffusion resistance, leading to ion aggregation and concentration polarization within pores and channels, which hinders the effective use of these micropores.^[18,19] In contrast, multilevel porosity with

[a] H. Zhou, Y. Gu, F. Liu, Prof. W. Wu

Laboratory of Thin Film Optics, Shanghai Institute of Optics and Fine Mechanics, Chinese Academy of Sciences, Shanghai 201800, China
and

State Key Laboratory of High Field Laser Physics, Shanghai Institute of Optics and Fine Mechanics, Chinese Academy of Sciences, Shanghai 201800, China

E-mail: guyunjiao@siom.ac.cn
wuw@siom.ac.cn

[b] H. Zhou

School of Microelectronics, Shanghai University, Shanghai 201800, China

 Supporting information for this article is available on the WWW under <https://doi.org/10.1002/batt.202400710>

structural disorder^[20] is more effective, as a balanced mix of mesopores and micropores in the carbon structure creates a three-dimensional pathway for efficient ion transport. Various pore-structure optimization strategies, including some proposed by our group,^[21,22] have been employed to achieve such structures. For instance, Coia et al.^[23] created hierarchical porosity from both carbon fibers (CFs) and covalent organic frameworks (COF) by grafting a range of COF scaffolds to the surface of CFs via a two-step functionalization. However, creating such porous structures is relatively complex and involves templating methods. Additional template removal, which often requires etching, is also an environmental concern.

Considering both aspects, we propose constructing in-situ N-doped hierarchical porous carbon through direct multilevel crosslinking of azobenzene-containing polyimide. Polyimides (PIs) are highly tunable polymer precursors for carbon material synthesis, offering diverse chemical structures, elemental compositions, and thermomechanical stability.^[23–26] Azobenzene-based molecules are commonly used as photoresponsive units,^[27] they are also redox-active, due to their conjugated structure with azo group connected with two phenol rings. Nevertheless, their applications in supercapacitor electrolytes, redox-flow batteries, and related energy storage scenarios are far less considered.^[28–30]

Here, we intend to incorporate azobenzene derivatives as a third building block in the PI skeleton. Such addition, which both increases in-situ N content and enables synergistic double-network crosslinking, will not only introduce additional pseudocapacitance through redox reaction but also enrich and promote hierarchical porosity during carbonization, thereby improving both the performance and stability of the resulting supercapacitors. To the best of our knowledge, there have been few reports on the incorporation of azobenzene into electrode materials, particularly polymer-based carbon materials, in supercapacitor applications.

In the study, we prepared N-doped multilevel porous carbon materials through one-pot polymerization of azobenzene-containing PI with in-situ dual-crosslinking network struc-

tures, using three crosslinking monomers—azobenzene-4,4'-dichloro dichloride (AZO), 4,4'-(hexafluoroisopropylidene) diphthalic anhydride (6FDA), and tetraethylenepentamine (TEPA)—followed by carbonization activation. The structure of the synthesized polymer precursor and the morphology of the subsequent carbonized material were thoroughly examined using FTIR, SEM, TEM, and XRD. The electrochemical performance was assessed using a three-electrode system to determine the specific capacitance at different current densities and evaluate cycling stability, highlighting its potential for advanced energy storage applications.

2. Results and Discussion

2.1. Synthesis of AFT Polymeric Precursor

The fabrication of NHPC materials begins with the synthesis of azobenzene-containing polyimide as the polymer precursor. The preparation process is illustrated in Figure 1(a). 6FDA, AZO, and TEPA were intentionally selected as the three building blocks of the azobenzene-containing polyimide network. Network formation is driven by nucleophilic reactions between amine groups of TEPA and anhydride groups of 6FDA, as well as acyl chloride groups of AZO. It is noteworthy that TEPA possesses both primary and secondary amine sites with different electrophilicity, capable of providing abundant reactive sites for dual-crosslinking and the formation of a three-dimensional network.

This one-pot synthesis of the polymer precursors was confirmed by FTIR, as demonstrated in Figure 2(a). For TEPA, the peak at 1303 cm^{-1} represents the C–N bond (stretching), and the peaks at 3355 cm^{-1} and 346 cm^{-1} represent primary/secondary amines. Within AZO, the strong signal at 1690 cm^{-1} corresponds to aromatic carbonyl groups (stretching), while the peak at 1780 cm^{-1} corresponds to $-\text{COCl}$ groups (stretching). As for 6FDA, the stretching vibration peaks of the anhydride split into two respectively at 1853 cm^{-1} and 1780 cm^{-1} . In contrast,

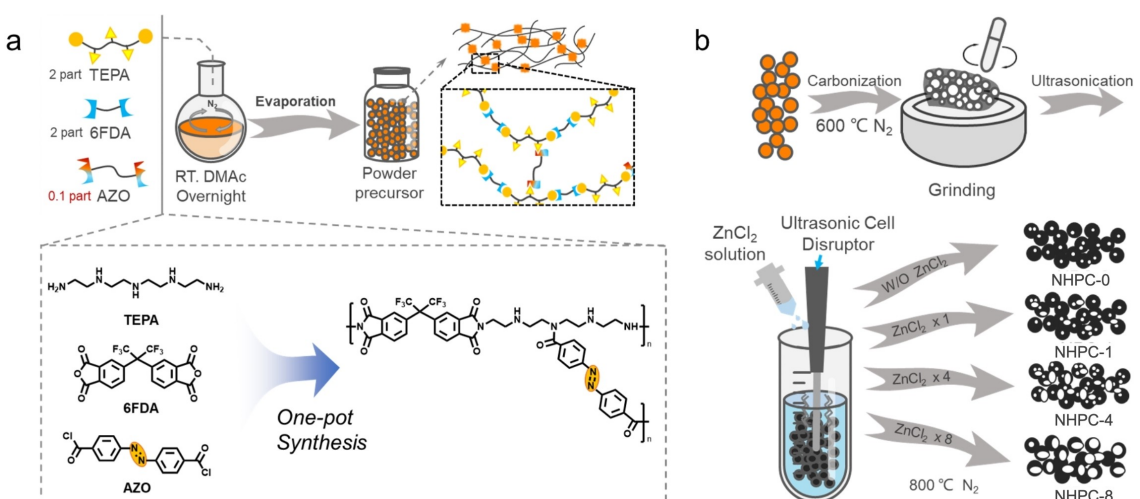


Figure 1. (a) Synthetic routes of polymer precursors and their chemical formulas, (b) fabrication of nitrogen-doped porous carbon materials.

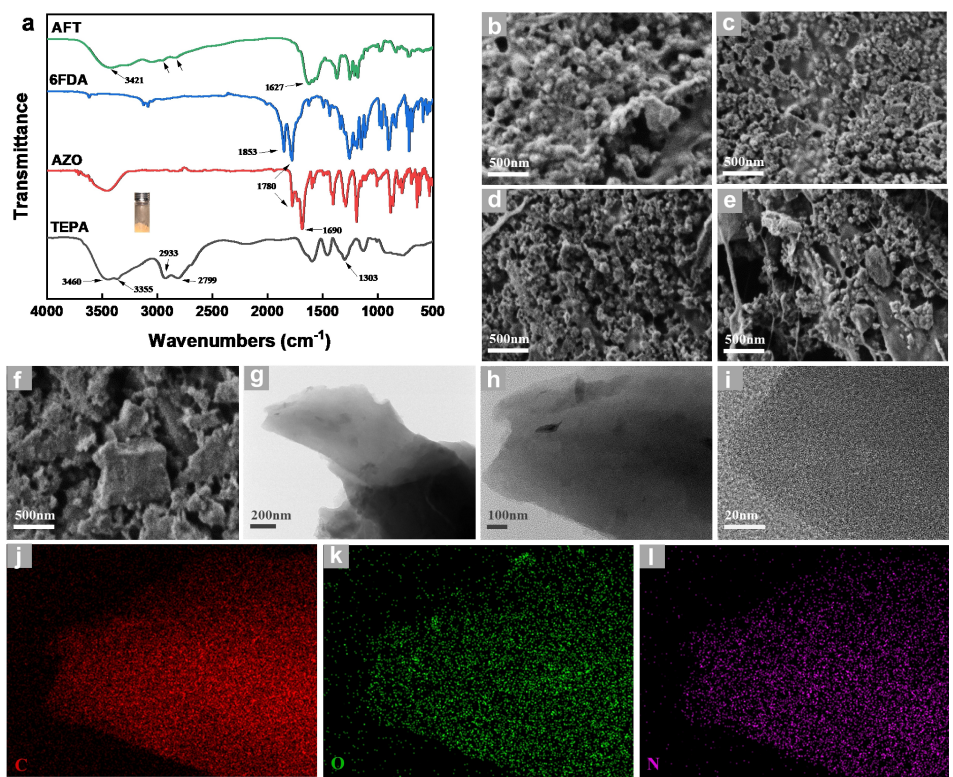


Figure 2. (a) The FTIR spectra of monomers and precursors, SEM images of porous carbon materials, (b–f) NHPC-0, NHPC-1, NHPC-4, NHPC-8 and NPC-0, TEM images of NHPC-4 at different magnifications (g–i) and EDS analysis images of (j–l) C, O, and N elements.

after the reaction, the characteristic peaks of the aforementioned monomer functional groups were all diminished and replaced by the absorption peaks at 1627 cm⁻¹ in the precursor polymer, indicating the formation of secondary amide groups, a signature of the polyimide formation. Also, the occurrence of the single peak at 3421 cm⁻¹ is an indication of N–H groups (stretching).^[31] The peaks observed in the 3000–2500 cm⁻¹ range, characteristic of the C–H (alkyl) stretching in TEPA, are also detected in the product AFT, confirming the successful reaction of TEPA into the AFT network. All these changes indicate the successful nucleophilic reaction and the formation of the tri-component dual-crosslinking azo-containing polyimide structures (Figure 1(a) dashed box). Notably, the orange color of the polymer precursor in the powder form (inset of Figure 2(a), Figure S1) is a distinctive feature resulting from the presence of azobenzene groups. In this precursor fabrication stage, AZO not only provides an additional nitrogen source for the carbon material, but also more importantly, enhances the overall cross-linking alongside TEPA, which will be critical for creating carbonization multilevel porosity during the subsequent carbonization process.

2.2. Fabrication of N-Doped Hierarchical Porous Carbon (NHPC)

The transition from polymer precursors into NHPCs involves two sequential processes, i.e., carbonization and activation. The

as-prepared AFT was first carbonized in a 600 °C tube furnace under a nitrogen atmosphere for lightweight porous carbon. To explore the undergoing decomposition process, the synchronous TGA-MS analysis was carried out to identify the pyrolysis products. According to the TG curve in Figure S2(a), the weight loss of AFT is continuously decreasing, with the fastest weight loss arriving at 520 °C. The major weight loss should be deduced from the continuous fragmentation of alkyl chains, according to the high ion current intensity of the fragments with a m/e ratio of 27 (–C₂H₅) from Figure S2(b). Signals in other MS curves before 600 °C should arise from the release of H₂O, CO₂, CH₄, –OH and so on,^[32–34] with a final weight loss of ~60%.

Thereafter, the as-obtained porous N-doped carbon was further activated with zinc chloride (Figure 1(b)). The morphology and structure of NHPC-0, NHPC-1, NHPC-4, NHPC-8, and NPC-0 are presented in Figure 2(b–f). As seen in Figure 2(b–e), all NHPC-x, including NHPC-0, exhibit hierarchical micro-/nano-scale porous structures. The concentrations of zinc chloride continuously increase from Figure 2(b) to 2(e). Correspondingly, with the increase of the activation degrees, the number of macropores on the material surface increases, accumulates and gradually extends into the interior of the carbon material. NHPC-4 in Figure 2(d) shows the richest hierarchical morphology, and over-activation for NHPC-8 leads to the overall pore size developing into larger scales and fewer hierarchical pores on the surface. Notably, the control sample NPC-0 with the exact same fabrication procedure but without AZO in Figure 2(f) shows much larger pore structures, which is also confirmed in

the following BET analysis in Figure 3(c). This phenomenon highlights the unique function of AZO, which is proven to trigger the formation of multi-scale porosity in the final product.

For a detailed study of NHPC-4, TEM images in Figure 2(g–h) reveal its higher resolution morphologies and the rich mesoporous and microporous structure of the NHPC-4 surface can be seen in Figure 2(i), which is also confirmed in the following BET analysis. This structure is advantageous for the improvement of its electrochemical performance, which will be displayed for discussion later. Homogeneous distribution of nitrogen (N) throughout the bulk phase, due to the in-situ doping of N, has been demonstrated by elemental distribution analysis in Figure 2(j–l). This is the key to the ultimate electrochemical improvement of the supercapacitor, which will be discussed in Section 2.3.

Figure 3(a) presents the Raman spectra of NHPC-x and NPC-0, showing two characteristic peaks, i.e., D peak at 1350 cm^{-1} and G peak at 1580 cm^{-1} . The D peak corresponds to sp^3 -hybridized carbon atom vibrations, while the G peak deals with sp^2 vibrations. The intensity ratio of D to G peaks (I_D/I_G) implies the degree of graphitization.^[35] As seen in Figure 3(a), the I_D/I_G ratio is close to 1, indicating partial graphitization in NHPC with some defects, which improves electron conductivity. The similar

Raman peak positions and intensities across samples with varying activation levels indicate that the activation process did not alter the chemical characteristics of the samples. Furthermore, XRD was performed on NHPC-x and NPC-0 (Figure 3(b)). Two peaks observed at 24.2° (strong) and 43.8° (weak) represent the (002) plane and (100) plane of graphite, respectively. The (100) plane reflects the arrangement of aromatic rings during the graphitization process,^[36] indicating a graphitic carbon network structure has been formed during the carbonization of the semi-aromatic three-dimensional polyimide. A decrease in peak intensity of NHPC-8 in the XRD profile suggests that this sample was over-activated, which resulted in less ordered structures.

The pore size distributions and nitrogen adsorption/desorption isotherms of NHPC-x are shown in Figures 3(c) and 3(d), respectively. From Figure 3(c), the pore distribution of NHPC-x is mainly in the microporous range ($<2\text{ nm}$). Conversely, NPC-0 exhibits both micropores and mesopores, with a much higher proportion of larger pores. This also agrees with the data from Table S1, where $V_{\text{micro}}/V_{\text{total}}$ for the control sample NPC-0 accounts for 65.87%, whilst the value increases to ~90% for those with AZO (i.e. NHPC-x). Therefore, it can be concluded that the addition of AZO reduces these large mesopores and increases the proportion of micropores.

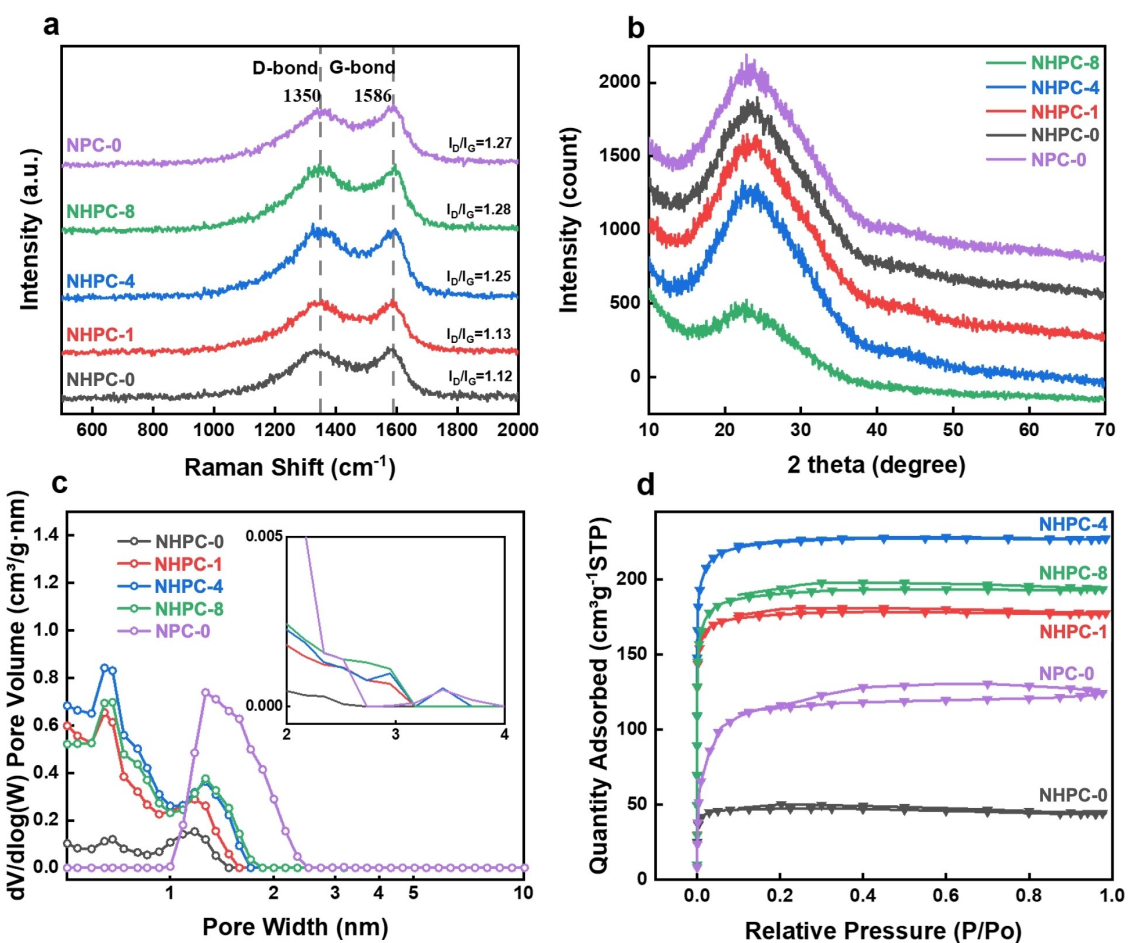


Figure 3. (a) The Raman spectra of NHPCs, (b) the XRD patterns of NHPCs, (c) the pore size distribution curves of NHPCs (inset: the magnified portion of 2–4 nm), (d) the Nitrogen adsorption-desorption isotherms.

From Figure 3(d), it can be observed that after activation with $ZnCl_2$ porosity increases, thereby nitrogen adsorption increases in NHPC-x ($x=1, 4, 8$). In the range of $0.3 < P/P_0 < 0.8$, NHPC-0, NHPC-1, NHPC-8, and NPC-0 exhibit hysteresis loops of varying sizes, which is the typical H4 of Type IV with distinct saturation adsorption plateaus. This suggests the presence of irregular pore structures. Interestingly, NHPC-4 exhibits the best saturated adsorption, as a typical Type I isotherm with the richest micropores aside from mesopores, which signifies the highest specific surface area of $900.1\text{ m}^2\text{ g}^{-1}$. This is later confirmed to be beneficial to the electrochemical performance of NHPC-4.

The elemental compositions of all NHPC-x samples were further analyzed using XPS in Figure 4(a) and Table S2. All samples demonstrate three distinct peaks at 285 eV, 400 eV, and 530 eV, respectively corresponding to the presence of C, N, and O elements. NHPC-4 was further selected to conduct high-resolution XPS analysis (Figure 4(b-d)). The high-resolution C1s spectrum of NHPC-4 displays 5 distinct peaks in Figure 4(b) from 284.5 eV to 288.9 eV, which correspond to C–N, C–C/C=C, C–O, C=O, and O=C=O groups, respectively. The O1s spectrum (Figure 4(c)) can be deconvoluted into 3 peaks (532.0 eV, 532.7 eV, 534.2 eV), respectively for C=O, C–OH/C–O–C, and COOH. The N1s spectrum (Figure 4(d)) displays 3 peaks at 400.4 eV (N-5, pyrrolic-N), 398.7 eV (N-6, pyridinic-N), and 401.6 eV (N-Q, graphitic-N or quaternary-N). N-6 and N-Q are connected to sp^2 carbon atoms, which contribute electrons to the π -conjugated carbon network, enhancing the electrical conductivity of NHPC-4. Additionally, N-Q facilitates interactions with electrolyte ions and the formation of the electric

double layer to boost capacitance, while N-5 enables active sites and contributes to capacitance through its pseudocapacitive effect.^[37]

2.3. Electrochemical Performances of NHPC Materials

Based on the chemical and structural analysis, NHPC-x materials introduce heteroatoms for active sites, and exhibit well-defined porous structures and favorable pore size distributions, which are advantageous for electrode materials in supercapacitor applications. After ensuring the electrical conductivity of NHPC materials (Figure S3(d,e), Table S3), the electrochemical properties were then evaluated in a three-electrode system.

Cyclic voltammetry (CV) curves of these NHPC-x materials obtained at various scanning rates from 5 to 500 mVs⁻¹ are summarized in Figure 5(a) and Figure S4. In general, the CV curves of NHPC-x exhibit shape deviation and have larger integrated areas than NPC-0. This is due to the introduction of azobenzene and enough activation by $ZnCl_2$, which increases the proportion of N and O for more active sites in NHPC-x. The largest integration area of NHPC-4 suggests a highly effective interaction between the ions within the electrode and the electrolyte material. Figure 5(b) and Figure S5 display the Galvanostatic charge-discharge (GCD) curves of NHPC-x and NPC-0 electrodes. It can be observed that all GCD curves approximate an isosceles triangle shape and show no obvious IR drop, indicating the reversible behavior and superior Coulombic efficiency of the prepared supercapacitor electrode materials. The specific capacitance (C_g) of NHPC-x and NPC-0

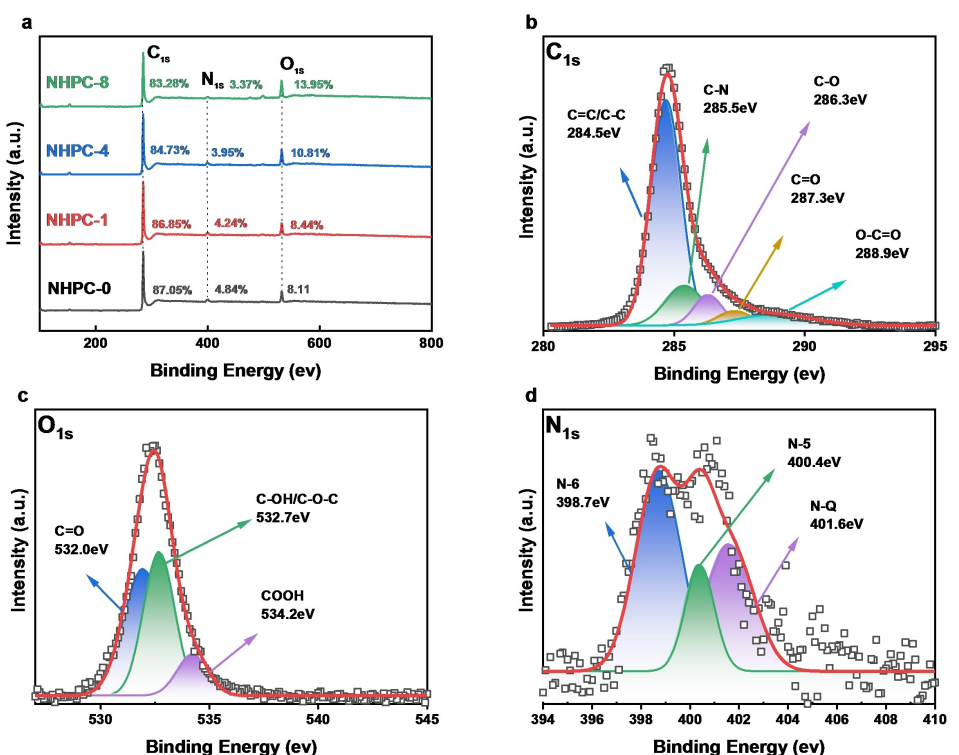


Figure 4. (a) The wide-scan XPS spectra of different NHPCs, and deconvoluted high-resolution elemental analysis of (b-d) C 1s, O 2p, N 1s for NHPC-4.

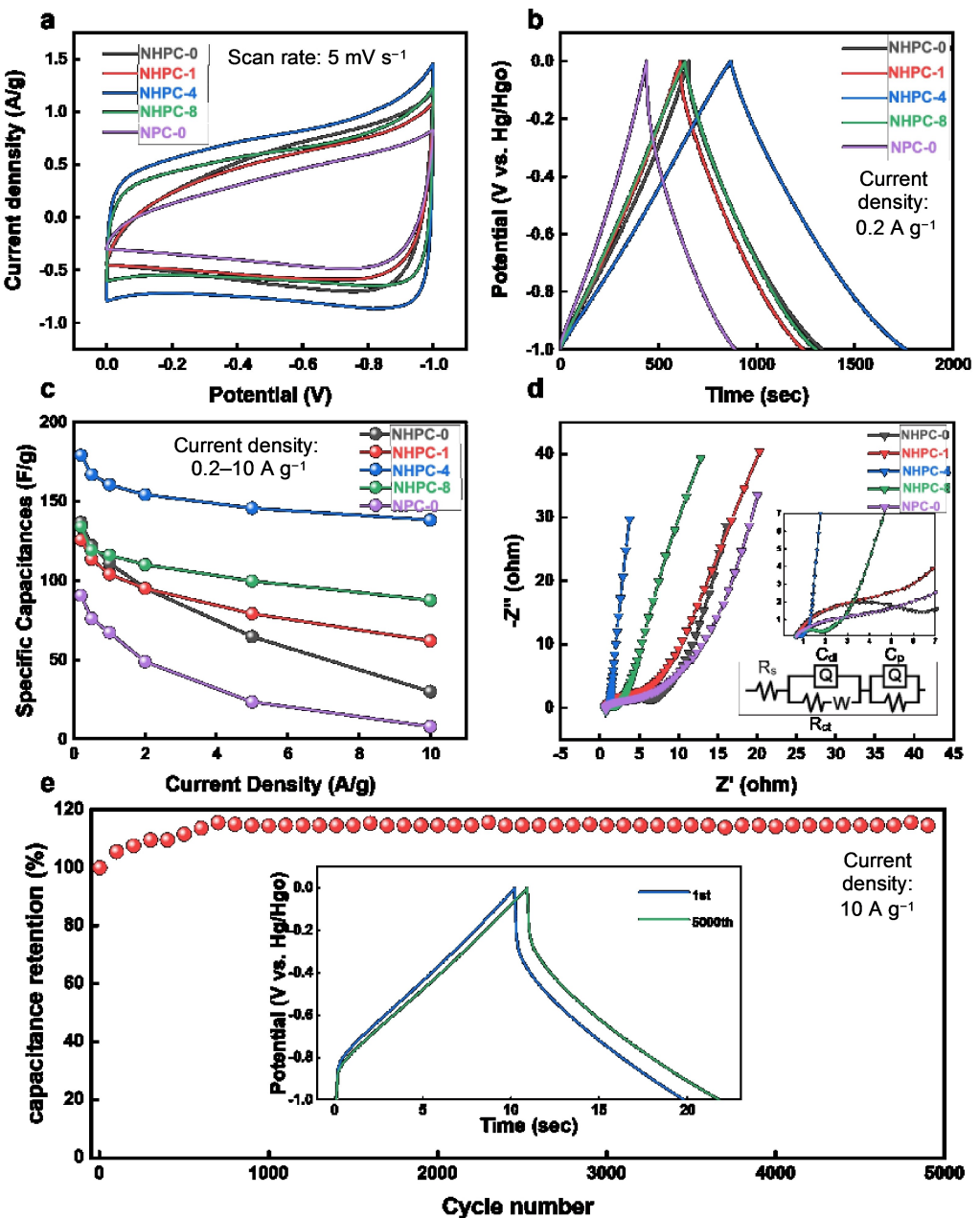


Figure 5. (a) CV curves, (b) GCD curves, (c) specific capacitance, (d) Nyquist plot of all 5 samples and the equivalent circuit diagram (R_s : the total contact resistance, including that of both active materials and electrolyte; C_d : the double-layer capacitance; C_p : the pseudocapacitance; R_{ct} : the charge-transfer resistance between the electrolyte and the electrode; W : the Warburg resistance. Inset: the magnified view of the low impedance regime), and (e) the cycling performance of the NHPC-4 for 5000 cycles (inset: comparison of the 1st and the last GCD cycles).

electrodes at different current densities was calculated from the GCD curves using the following formula,

$$C_g = \frac{I \times \Delta t}{m \times \Delta V} \quad (1)$$

where I represents the electric current, Δt denotes the discharge time, m stands for the mass of the fabricated material, and ΔV represents the range of electric potential.

According to Figure 5(c) and Table S4, under all current densities ($0.2\text{--}10\text{ A g}^{-1}$), NHPC-4 exhibits the highest specific

capacitance (138.2 F g^{-1} @ 10 A g^{-1}) compared to other materials. This is because the activated material has generated micro-pores, which enlarges charge storage and facilitates efficient interaction between ions and micropores under high current conditions. Furthermore, the specific capacitance of the control sample NPC-0 is significantly lower in both magnitude and decay rate. This can be attributed to the large mesopores, which exhibit extremely low efficiency of charge interaction at a high current density. It also indicates two contributions of AZO monomers: (1) Denser crosslinking of the AFT polymer precursor results in finer microporous structures after activation

for better double layer capacitance. (2) Increase of the N and O contents contributes to the pseudocapacitance increase.

The resistance and charge transfer kinetics of the electrodes are investigated by EIS in Figure 5(d) with the fitted equivalent circuit. The Nyquist plots consist of two parts, the straight line at the low-frequency (f) region, and the semicircle at the high- f region (Figure 5(d) inset). A steeper slope in the low-frequency region indicates more favorable ion diffusion and interaction with the electrode material in the electrolyte. A smaller semicircle radius in the high-frequency region signifies lower charge transfer resistance and ion diffusion impedance during charge-discharge processes. Among them, NHPC-4 exhibits the steepest slope and the smallest semicircular radius. This implies the lowest particle diffusion impedance and charge transfer impedance during charge-discharge processes. The lowered performance of NHPC-8 could be related to worse porosity due to over-activation. As shown in the capacitance-frequency relationship in Figure S6, the real part of the capacitance (C') increases as the alternating current frequency decreases (from 10 Hz to 0.01 Hz) and becomes less dependent on frequency. At the lowest frequency, C' reaches its highest value, with NHPC-4 exhibiting a maximum capacitance as high as 3.31 F cm^{-1} .

To explore the possibility of NHPC as the electrode active material in practical application scenarios, the cyclic stability of the NHPC-4 electrode material was evaluated by charge-discharge cycling. From Figure 5(e), the capacitance retention is stabilized at a high level without decrease throughout the GCD test over 5000th cycles. Interestingly, the capacitance even gradually increased in the first ~ 700 cycles. This can be reasonably explained by the presence of many unimpregnated micropores in the initial NHPC-4. As the cycle number increases, more utilized pores participate in the charge interaction process, resulting in a capacitance increase. Similar phenomena were also observed in the studies by Chang^[38] and Han.^[39] Excellent stability of NHPC-4 was observed in Figure 5(e), with the capacitance value of the last cycle stabilizing and reaching 113.5% of the initial capacitance value.

The reaction kinetics and energy storage mechanisms of NHPC-4 were further examined through CV analyses at various scan rates (Figure 6(a)). The current response rises with the scan rate increase due to the simultaneous occurrence of Faradaic and non-Faradaic processes within the NHPC-4 pore structure. Nevertheless, the rectangular CV shapes of the curves become more deformed with the scan rate increase, indicating a weakening interaction between the electrolyte ions and the pores in NHPC-4, which accounts for the reduced specific capacitance when the scan rate accelerates.

The reaction kinetics are evaluated from the following relationship,^[40]

$$i = av^b \quad (2)$$

where i represents the current density, and v is the potential sweep rate. The parameters a and b are variable, with b fitted from the plot in Figure 6(b). The b -value of 0.5 indicates a diffusion-controlled process, while 0.5 suggests a capacitive-controlled process. Since the b values for both anodic and

cathodic peaks in Figure 6(b) approach 1.0, this well suggests that charge storage in NHPC-4 is primarily governed by a fast capacitive process.

The quantitative contributions of capacitive and diffusion-controlled processes to the entire charge storage can be further calculated from the following equations,

$$i = mv + nv^{1/2} \quad (3)$$

$$\frac{i}{v^{1/2}} = mv^{1/2} + n \quad (4)$$

where i is the response current density at the potential v , mv represents the capacitive process, and $nv^{1/2}$ equals the diffusion-controlled processes. The values of m and n are derived from the plot of $i/v^{1/2}$ against $v^{1/2}$ (Figure S7). As shown in Figure 6(c), NHPC-4 exhibits a 62% Faradaic diffusion contribution when scanning at the rate of 5 mVs^{-1} . As the rate increases, the contribution of diffusion-controlled capacitance gradually decreases (Figure 6(d), Figure S8). At the largest scan rate (500 mVs^{-1}), the contribution of pseudocapacitance drops to 12%. This indicates that the kinetics of redox processes are slower relative to the increase in scan rate, also noted in ref.^[41]

The outstanding electrochemical properties of NHPC-4 can be explained by both the well-designed molecular structure of the polymer precursors and the formation of an N-doped multiscale porous structure after carbonization activation. Firstly, the precursor's molecular structure significantly enhances the conductivity of the NHPC material. The reaction among aliphatic and aromatic monomers forms a semi-aromatic three-dimensional skeleton, which leads to decarbonization and C–N bond cleavage in amide rings under high-temperature thermal treatment.^[42] This results in the merging of heterocycles and the formation of continuous aromatic heterocyclic compounds, resembling a graphitic carbon network. Such graphitic structure, confirmed by Raman spectroscopy and XRD analysis, is the key feature of conductive materials.

Secondly, the small amount of azobenzene-derivatives in our design not only acts as an additional in-situ nitrogen source, ensuring uniform nitrogen distribution in NHPCs to enhance the utilization of nitrogen-containing redox sites but also promotes polymer phase heterogeneity, leading to a hierarchical, highly porous structure after activation. The micropores enhance the contact surface area with the electrolyte, leading to a substantial enhancement in double-layer capacitance. The mesopores facilitate efficient ion transport, promoting the diffusion of ions to nitrogen-containing redox sites. Meanwhile, the macropores serve as ion reservoirs, shortening the distance of the moving electrolyte ions and improving overall charge storage efficiency. These design features collectively ensure the production of a high-quality, stable electrode material for supercapacitors. We further made a comparison of NHPC-4 with previously reported materials (Figure 6(e) and Table S5, ref.).^[13,17,43–55] Notably, all references are selected within the scope of N-doped porous carbon, underscoring the exceptional performance and stability of NHPC-4 due to its distinct physical and chemical structural advantages.

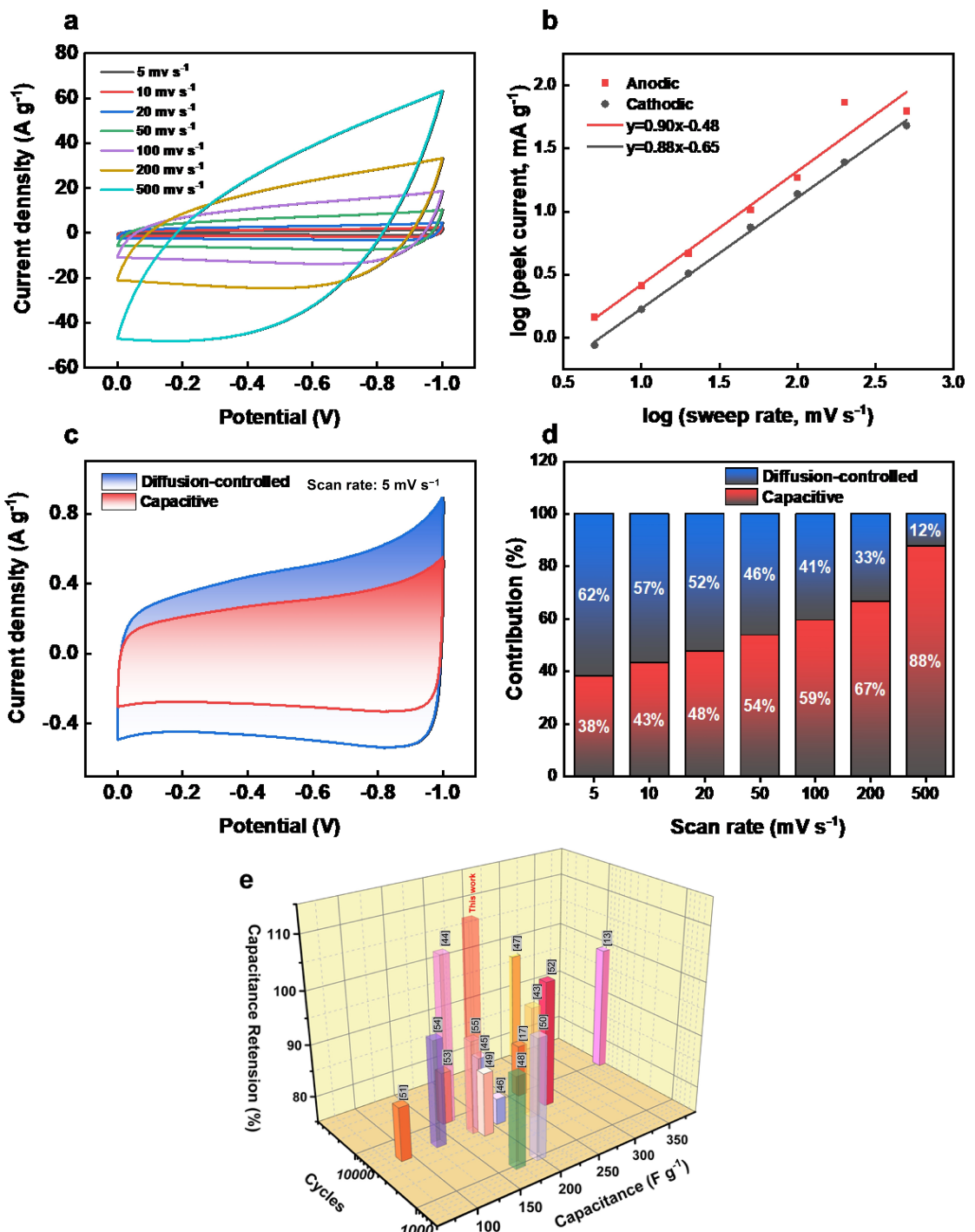


Figure 6. (a) The CV results of NHPC-4 at various scan rates, (b) the fitted $\log(i)$ vs. $\log(v)$ plots of both anodic and cathodic peaks, (c) separation of capacitive and diffusion-controlled current density results for the NHPC-4 electrode, (d) contribution percentages of the two charge storage types at various scan rates, and (e) comparison of the performance of NHPC-4 with existing reports.

The energy storage level of NHPCs was finally inspected by assembling a symmetric supercapacitor system, with NHPC-4 serving as the active material for both electrodes in a 6 M KOH solution. First, optimization of the working voltage window in Figure 7(a) shows that even at a potential window of 1.6 V, the CV curve maintained a quasi-rectangle shape, indicating strong capacitive behavior and rapid charge/discharge capabil-

ities. Nonetheless, at 1.7 V, a sharp increase in current has been observed due to electrolyte decomposition, thus leading to electrode polarization at high potentials, according to ref. [56]. Therefore, the voltage window of the symmetric supercapacitor is carried out within 0–1.6 V.

The quasi-rectangle shape of the CV curves in Figure 7(b) implies strong double-layer capacitance. Deviation in the CV

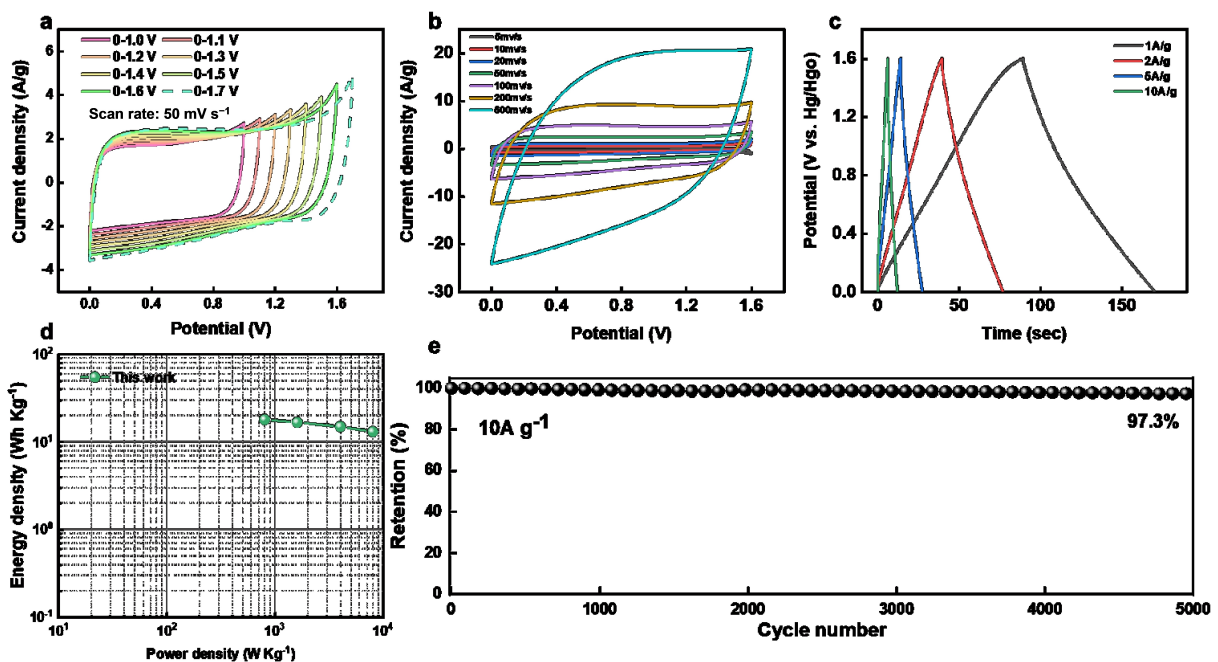


Figure 7. (a) The CV curves within a range of potential windows (1.0–1.7 V), (b) CV plots under various scan rates, (c) GCD curves of the assembled symmetric supercapacitors at various current densities, (d) Ragone plot of energy-power relationship, and (e) cycling durability at 10.0 A g^{-1} over 5000 cycles.

curves and slight distortion of the triangle shape in the GCD curves (Figure 7(c)) confirm the double-layer capacitance, accompanied by pseudocapacitance from faradic reactions at nitrogen-doped active sites for this symmetric supercapacitor. Capacitance at various current densities was calculated based on Equation 3 (Figure S9).

The Ragone plot in Figure 7(d) visualizes the tradeoff between power density and energy density of the NHPC-4 symmetric supercapacitor, where the energy density (E) and power density (P) are calculated by the following equations,

$$E = \frac{C_g \Delta V^2}{2 \times 3.6} \quad (5)$$

$$P = 3600 \frac{E}{\Delta t} \quad (6)$$

where C_g is the specific capacitance, ΔV is the voltage window, and Δt is the discharge time. At the current density of 1 A g^{-1} , the energy density reaches 18.0 Wh Kg^{-1} with a power density of 799.51 W Kg^{-1} , while at 10 A g^{-1} , the energy density decreases to 13.09 Wh Kg^{-1} with a power density of $7986.44 \text{ W Kg}^{-1}$. The device also demonstrates excellent cycling stability at large current densities (10 A g^{-1}), retaining 97.3% of its capacitance after 5000 charge-discharge cycles, according to Figure 7(e). These strong performance metrics validate the efficacy of our tailored precursor design.

3. Conclusions

To summarize, we have developed a novel strategy for fabricating template-free N-doped hierarchical porous carbon from in-situ dual-crosslinking azobenzene-containing polyimide precursors. Azobenzene-based molecules, traditionally used as photoresponsive agents, were ingeniously incorporated into the design of supercapacitor electrode material for the first time. These molecules not only enrich the N-content within the network but also enable the rapid formation of hierarchical porosity through the multilevel crosslinking reactions within the azobenzene-containing polyimide precursors, resulting in a large specific surface area and well-defined pore channels. N-doping contributes to pseudo-capacitance, enhancing the overall capacitance, while the hierarchical porosity provides a three-dimensional pathway for ion transportation, leading to impressive cycling stability and charge-discharge efficiency as the supercapacitor electrode material. Electrochemical tests show that the NHPC-4, obtained under optimal activation conditions, demonstrates high specific capacitance (179.2 F g^{-1}) and remarkable cycling stability (113.5% of the initial capacitance value) without performance degradation after 5000 cycles. The proof-of-concept demonstration of NHPC-4 in symmetric supercapacitors, with high capacitance retention after extended charge-discharge cycles, confirms its viability as an electrode material for practical applications. This work presents a new alternative to the design of tailor-made heteroatom-doped carbon-based supercapacitor electrode materials, offering valuable insights and guidance for the future development of ultra-stable and high-performance supercapacitors.

Acknowledgements

This work was supported by the National Natural Science Foundation of China (52273242, 22202231), the National Key R&D Program of China (2021YFB2800703, 2021YFB2800701) and the Chinese Academy of Sciences.

Conflict of Interests

The authors declare no conflict of interest.

Data Availability Statement

The data that support the findings of this study are available from the corresponding author upon reasonable request.

Keywords: azobenzene · double crosslinking · nitrogen-doped · porous carbon · supercapacitors

- [1] Y. Zhou, H. Qi, J. Yang, Z. Bo, F. Huang, M. S. Islam, X. Lu, L. Dai, R. Amal, C. H. Wang, Z. Han, *Energy Environ. Sci.* **2021**, *14*, 1854.
- [2] N. Kittner, F. Lill, D. M. Kammen, *Nat. Energy* **2017**, *2*, 17125.
- [3] X. Xu, H. Qu, Y. Wang, C. Wang, S. Wu, C. Wang, *Small* **2024**, 2405371.
- [4] G. Shao, R. Yu, N. Chen, M. Ye, X. Y. Liu, *Small Methods* **2021**, *5*, 2000853.
- [5] F. Sun, D. Wu, J. Gao, T. Pei, Y. Chen, K. Wang, H. Yang, G. Zhao, *J. Power Sources* **2020**, *477*, 228759.
- [6] Q. Zhu, D. Zhao, M. Cheng, J. Zhou, K. A. Owusu, L. Mai, Y. Yu, *Adv. Energy Mater.* **2019**, *9*, 1901081.
- [7] S. Liu, L. Wei, H. Wang, *Appl. Energy* **2020**, *278*, 115436.
- [8] J. Noh, S. Jekal, C. Yoon, *Adv. Sci.* **2023**, *10*, 2301923.
- [9] C. Wang, L. Zhang, Z. Zhang, R. Zhao, D. Zhao, R. Ma, L. Yin, *Prog. Mater. Sci.* **2021**, *118*, 100763.
- [10] T. B. Nguyen, B. Yoon, T. D. Nguyen, E. Oh, Y. Ma, M. Wang, J. Suhr, *Carbon* **2023**, *206*, 383.
- [11] T. Wang, R. Pan, M. L. Martins, J. Cui, Z. Huang, B. P. Thapaliya, C. L. Do-Thanh, M. Zhou, J. Fan, Z. Yang, M. Chi, T. Kobayashi, J. Wu, E. Mamontov, S. Dai, *Nat. Commun.* **2023**, *14*, 4607.
- [12] D. Dong, Y. Xiao, *Chem. Eng. J.* **2023**, *470*, 144441.
- [13] X. Gang, M. Krishnamoorthy, W. Jiang, J. Pan, Z. Pan, X. Liu, *Carbon* **2021**, *171*, 62.
- [14] L. Yang, X. Guo, Z. Jin, W. Guo, G. Duan, X. Liu, Y. Li, *Nano Today* **2021**, *37*, 101075.
- [15] Z. Sheng, X. Lin, H. Wei, Y. Zhang, Z. Tian, C. Wang, D. Xu, Y. Wang, *J. Power Sources* **2021**, *515*, 230629.
- [16] X. L. Dong, L. Hou, X. Hu, Y. T. Wu, L. Y. Dong, X. F. Yu, G. P. Hao, A. H. Lu, *EnergyChem* **2023**, *5*, 100099.
- [17] J. Du, A. Chen, L. Liu, B. Li, Y. Zhang, *Carbon* **2020**, *160*, 265.
- [18] N. Ganfoud, A. Sene, M. Haefele, A. Marin-Lafleche, B. Daffos, P. L. Taberna, M. Salanne, P. Simon, B. Rotenberg, *Energy Storage Mater.* **2019**, *21*, 190.
- [19] R. Mendoza, J. Oliva, V. Rodriguez-Gonzalez, *Int. J. Energy Res.* **2022**, *46*, 6989.
- [20] X. Liu, D. Lyu, C. Merlet, M. J. A. Leesmith, X. Hua, Z. Xu, C. P. Grey, A. C. Forse, *Science* **2024**, *384*, 321.
- [21] X. Xu, F. Liu, H. Zhou, Y. Wang, Y. Gu, W. Wu, *Solar RRL* **2024**, *8*, 2300846.
- [22] L. Wang, F. Liu, B. Zhao, Y. Ning, L. Zhang, R. Bradley, W. Wu, *ACS Appl. Nano Mater.* **2020**, *3*, 6448.
- [23] P. Coia, B. Dharmasiri, D. J. Hayne, A. Borkar, C. Hua, E. Austria, B. Akhavan, M. A. N. Judicpa, K. A. S. Usman, J. Razal, L. C. Henderson, *Small Structures* **2024**, *5*, 2400166.
- [24] Z. Lu, F. Sui, Y. E. Miao, G. Liu, C. Li, W. Dong, J. Cui, T. Liu, J. Wu, C. Yang, *J. Energy Chem.* **2021**, *58*, 170.
- [25] X. Li, J. He, Y. Liao, S. Zhu, Y. Tang, H. Li, N. Lv, Y. Xu, Y. Wang, *J. Power Sources* **2022**, *525*, 231124.
- [26] H. Li, L. Cao, H. Zhang, Z. Tian, Q. Zhang, F. Yang, H. Yang, S. He, S. Jiang, *J. Colloid Interface Sci.* **2022**, *609*, 179.
- [27] F. A. Jerca, *Nat. Chem. Rev.* **2022**, *6*, 51.
- [28] P. N. Singh, M. G. Mohamed, S. W. Kuo, *ACS Appl. Energ. Mater.* **2023**, *6*, 11342.
- [29] Y. Zhao, *Chem. Commun.* **2022**, *58*, 11567.
- [30] L. Zhang, *Nat. Commun.* **2020**, *11*, 3843.
- [31] C. Huang, X. Sun, H. Yuan, C. Song, Y. Meng, X. Li, *Vib. Spectrosc.* **2020**, *106*, 102993.
- [32] W. Xie, R. Heltsley, X. Cai, F. Deng, J. Liu, C. Lee, W. Pan, *J. Appl. Polym. Sci.* **2002**, *83*, 1219.
- [33] N. Pakusong, J. Pfersich, P. J. Arauzo, D. Jung, A. Kruse, *ACS Omega* **2020**, *5*, 12210.
- [34] K. Pielichowski, J. Njuguna, T. M. Majka, in *Thermal Degradation of Polymeric Materials (Second Edition)* (Eds: K. Pielichowski, J. Njuguna, T. M. Majka), Elsevier, **2023**, pp. 9–11.
- [35] Y. Katsuyama, N. Haba, H. Kobayashi, K. Iwase, A. Kudo, I. Honma, R. B. Kaner, *Adv. Funct. Mater.* **2022**, *32*, 2201544.
- [36] T. Kato, Y. Yamada, Y. Nishikawa, H. Ishikawa, S. Sato, *Carbon* **2021**, *178*, 58.
- [37] Z. Song, D. Zhu, L. Li, T. Chen, H. Duan, Z. Wang, Y. Lv, W. Xiong, M. Liu, L. Gan, *J. Mater. Chem. A* **2019**, *7*, 1177.
- [38] B. Chang, Y. Wang, K. Pei, S. Yang, X. Dong, *RSC Adv.* **2014**, *4*, 40546.
- [39] G. Han, J. Jia, Q. Liu, G. Huang, B. Xing, C. Zhang, Y. Cao, *Carbon* **2022**, *186*, 380.
- [40] W. Lu, J. Shen, P. Zhang, Y. Zhong, Y. Hu, X. W. Lou, *Angew. Chem. Int. Ed.* **2019**, *58*, 15441.
- [41] Y. K. Kim, J. H. Park, J. W. Lee, *Carbon* **2018**, *126*, 215.
- [42] Z. Chen, S. Zhang, Q. Feng, Y. Wu, S. Liu, J. Zhao, *Macromol. Chem. Phys.* **2020**, *221*, 2000085.
- [43] D. C. Guo, J. Mi, G. P. Hao, W. Dong, G. Xiong, W. C. Li, A. H. Lu, *Energy Environ. Sci.* **2013**, *6*, 652.
- [44] Y. Liu, L. Cao, J. Luo, Y. Peng, Q. Ji, J. Dai, J. Zhu, X. Liu, *ACS Sustainable Chem. Eng.* **2019**, *7*, 2763.
- [45] P. Thirukumaran, R. Atchudan, A. Shakila Parveen, M. Santhamoothry, V. Ramkumar, S. C. Kim, *Polymer* **2021**, *13*, 13.
- [46] D. Yan, D. C. Guo, A. H. Lu, X. L. Dong, W. C. Li, *J. Colloid Interface Sci.* **2019**, *557*, 519.
- [47] W. Jiang, J. Cai, J. Pan, S. Guo, Y. Sun, L. Li, X. Liu, *J. Power Sources* **2019**, *432*, 102.
- [48] L. Bai, Y. Ge, L. Bai, *Coating* **2019**, *9*, 10.
- [49] H. R. Abuzeid, A. F. M. El-Mahdy, M. M. M. Ahmed, S. W. Kuo, *Polym. Chem.* **2019**, *10*, 6010.
- [50] M. Zhang, M. Chen, N. Reddeppa, D. Xu, Q. Jing, R. Zha, *Nanoscale* **2018**, *10*, 6549.
- [51] J. Xia, N. Zhang, S. Chong, D. Li, Y. Chen, C. Sun, *Green Chem.* **2018**, *20*, 694.
- [52] J. Li, Q. Wu, *Chem. Phys. Lett.* **2018**, *691*, 238.
- [53] M. Karnan, K. Subramani, P. K. Srividhya, M. Sathish, *Electrochim. Acta* **2017**, *228*, 586.
- [54] S. He, H. Hou, W. Chen, *J. Power Sources* **2015**, *280*, 678.
- [55] L. Jiang, J. Yan, L. Hao, R. Xue, G. Sun, B. Yi, *Carbon* **2013**, *56*, 146.
- [56] H. Chen, H. Wei, N. Fu, W. Qian, Y. Liu, H. Lin, S. Han, *J. Mater. Sci.* **2018**, *53*, 2669.

Manuscript received: November 10, 2024
Revised manuscript received: December 17, 2024
Accepted manuscript online: December 24, 2024
Version of record online: January 8, 2025